A&A, 700, A54 (2025)
https://doi.org/10.1051/0004-6361/202554338

Astronomy & Astrophysics

Spiral galaxies with unusual azimuthal asymmetry in oxygen abundance

L. S. Pilyugin[1,2,⋆] and G. Tautvaišienė[1]

[1] Institute of Theoretical Physics and Astronomy, Vilnius University, Sauletekio av. 3, 10257 Vilnius, Lithuania
[2] Main Astronomical Observatory, National Academy of Sciences of Ukraine, 27 Akademika Zabolotnoho St, 03680 Kiev, Ukraine

Received 1 March 2025 / Accepted 3 June 2025

ABSTRACT

We considered five galaxies in the Mapping Nearby Galaxies at the Apache Point Observatory (MaNGA) survey that show distinct azimuthal asymmetry in the abundance, in the sense that in the inner part (more than half of the optical radius, R_{25}) of each galaxy there is a sector-like (up to semi-circle) region where the oxygen abundances $(\mathrm{O/H})_\mathrm{h}$ are higher than the abundances $(\mathrm{O/H})_\mathrm{l}$ in other sector. M-11761-12705 is a massive galaxy with a stellar mass of $\log(M_\star/M_\odot) = 11.6$; the masses of four other galaxies (M-8450-12701, M-8546-12704, M-8561-12701, M-9500-09102) are moderate: $10.1 \lesssim \log(M_\star/M_\odot) \lesssim 10.4$. Abundances within both high- and low-metallicity regions show flat radial gradients (the abundances are at nearly constant levels). The histogram for the spaxel abundances demonstrates two distinct peaks, the difference between the $(\mathrm{O/H})_\mathrm{h}$ and the $(\mathrm{O/H})_\mathrm{l}$ abundances are of 0.06–0.08 dex. The high-metallicity regions are located in the O/H – N/O diagram closer to the lower envelope of the band than the low-metallicity regions. The abundance properties in the massive galaxy M-11761-12705 can be explained by the low-metallicity gas infall onto the galaxy and subsequent episode of high star formation rate (starburst) in the diluted interstellar medium occurring between 20 Myr $\lesssim t \lesssim$ 50 Myr ago. For moderate-mass galaxies, the higher oxygen abundance in the high-metallicity region and its shift towards the lower envelope in the N/O – O/H diagram compared to the low-metallicity region can be explained in one of two ways: either the starburst in the high-metallicity region occurred several dozens of Myr ago, or the star formation in the galaxy is accompanied by galactic winds, and the region evolved with the lower efficiency of the enriched galactic winds shows higher metallicity. Two galaxies of our sample (M-8546-12704 and M-11761-12705) are members of galaxy pairs. However, the asymmetry parameter, A, quantifying the asymmetry of a light distribution across the galaxy, is above the canonical threshold ($A = 0.35$) between non-interacting and interacting galaxies in the massive galaxy M-11761-12705 only. The values of the A parameter in four moderate-mass galaxies (including a member of the galaxy pair) are below the threshold value.

Key words. galaxies: abundances – galaxies: ISM – galaxies: spiral

1. Introduction

The discs of spiral galaxies have long been known to show negative radial abundance gradients in the sense that the abundance is higher at the centre and decreases with the galactocentric distance (Searle 1971; Smith 1975). The distribution of nebular abundances across the disc of a galaxy is specified by a relation between the oxygen abundance, O/H, and the galactocentric distance, R. Relations of this type were determined for many galaxies by different authors (Vila-Costas & Edmunds 1992; Zaritsky et al. 1994; Pilyugin et al. 2004, 2007, 2014, 2019; Gusev et al. 2012; Sánchez et al. 2014; Ho et al. 2015; Sánchez-Menguiano et al. 2016; Belfiore et al. 2017; Sánchez-Menguiano et al. 2018; Kreckel et al. 2019; Berg et al. 2020; Pilyugin & Tautvaišienė 2024, among many others).

It is a common practice to derive the relation between the oxygen abundance, O/H, and the galactocentric distance, R, assuming that the abundance within the disc is symmetric. Numerical simulations predict azimuthal variations in abundances (e.g. Grand et al. 2016; Bellardini et al. 2021, 2022; Orr et al. 2023). Integral field unit (IFU) spectroscopy of galaxies provides the possibility of constructing the abundance map and investigating the azimuthal variations in metallicity within the disc. The uncertainties in the abundance determinations (e.g. due to uncertainties in the emission lines measurements, uncertainties in the calibrations used in the abundance determinations, and contamination of the H II region spectra by the non-stellar (shochs) ionising radiation) can make a contribution to the scatter in the measured oxygen abundances at a given radius. Sánchez et al. (2015) analysed the abundance distribution across the galaxy NGC 6754 using the IFU spectroscopy obtained with the Multi Unit Spectroscopic Explorer (MUSE) and found evidence of an azimuthal variation in the oxygen abundance with an amplitude of ~0.05 dex. Zinchenko et al. (2016) constructed maps of the oxygen abundance across the discs of 88 galaxies using observations obtained by the CALIFA survey (Calar Alto Legacy Integral Field Area survey; Sánchez et al. 2012). They found that the scatter in oxygen abundances around the abundance gradient is within 0.05 dex. Ho et al. (2018) found 0.06 dex azimuthal variations in the oxygen abundance in NGC 2997. At a given radial distance, the oxygen abundances are higher in the spiral arms and lower in the inter-arm regions. Mapping both the radial and azimuthal variations in metallicity across a sample of galaxies is a key science goal of the PHANGS (Physics at High Angular Resolution in Nearby GalaxieS) project. Kreckel et al. (2019) mapped the two-dimensional distribution of the gas-phase oxygen abundances

---

⋆ Corresponding author.

for 7138 H II regions across the discs of eight nearby galaxies using Very Large Telescope/Multi Unit Spectroscopic Explorer (MUSE) optical integral field spectroscopy obtained within the PHANGS project. They found a very small root-mean-square scatter in residual metallicity (0.03–0.05 dex) after subtracting the radial gradients. Grasha et al. (2022) determined oxygen abundances in a spatially resolved H II regions in six local star-forming and face-on spiral galaxies. They found a negative relation between the gas-phase oxygen abundance and galactocentric distance. All metallicity radial profiles were well approximated with a simple linear metallicity gradient with a small (mean 0.03 dex) scatter. NGC 1566 was an exception, with a significant scatter and a hint of flattening of the radial metallicity profile beyond 15 kpc from the galactic centre. Bellardini et al. (2021) examined variations of gas-phase oxygen abundances using simulations for Milky Way and M31-mass galaxies across their formation histories at $z \leqq 1.5$ (look-back time $\leqq$9.4 Gyr). They found that over time the azimuthal variations become weaker; azimuthal variations are typically 0.14 dex at $z = 1$ and become as small as 0.05 dex at $z = 0$.

In some cases, the azimuthal variations in the oxygen abundance can be attributed to the spiral arms (Sánchez-Menguiano et al. 2017; Sakhibov et al. 2018; Ho et al. 2018; Kreckel et al. 2019; Sánchez-Menguiano et al. 2020). However, Kreckel et al. (2019) found, for eight PHANGS galaxies, that azimuthal variations are not always obviously associated with the spiral pattern. In all cases, the azimuthal trends are more pronounced on only one spiral arm. Williams et al. (2022) examined the 2D variations in metals across the discs of 19 PHANGS galaxies and found no evidence that spiral arms are enriched compared to the disc. Sánchez-Menguiano et al. (2020) found the presence of more metal-rich H II regions in the spiral arms with respect to the corresponding interarm regions for 45–65% of galaxies while 5–20% of galaxies display the opposite trend; i.e. more metal-poor H II regions are in the spiral arms compared to the inter-arm regions.

Kreckel et al. (2019) noted that H II regions with enhanced or reduced metallicity are located across the full disc. Grasha et al. (2022) also found that H II regions with enhanced and reduced abundances are distributed throughout the whole disc. Thus, spiral galaxies reveal an azimuthal variation in the oxygen abundance with an amplitude within ~0.05 dex, and regions with enhanced and reduced abundances are distributed throughout the whole disc.

We found five galaxies in the Mapping Nearby Galaxies at Apache Point Observatory survey (MaNGA, Bundy et al. (2015)) with unusual abundance distributions. In the inner (more than half of the optical radius) part of each galaxy, there is a large, sector-like (up to a semi-circle) region where the oxygen abundances are appreciably higher ($\gtrsim$0.06 dex) than in another sector, that is, the difference between the oxygen abundances in those sectors exceed the typical value of the scatter around the O/H – R relations and an amplitude of the reported azimuthal variations in the oxygen abundance (e.g. Sánchez et al. 2012; Zinchenko et al. 2016; Kreckel et al. 2019; Grasha et al. 2022). An azimuthal asymmetry of this kind cannot be attributed to the spiral arms. The study of such galaxies can shed light on some aspects of the (chemical) evolution of galaxies. This paper is organised as follows: the oxygen abundance and other characteristics of selected galaxies are described in Sect. 2; the analysis of the parameters of these galaxies and the discussion of possible way(s) of the formation of the abundance distributions are given is in Sect. 3; and Sect. 4 contains a brief conclusion.

2. Data and galaxy sample

2.1. Data

Our investigation is based on galaxies from the MaNGA survey (Bundy et al. 2015). The completed observations of MaNGA galaxies were included in Data Release 17 (Abdurro'uf et al. 2022). The MaNGA data products were also revised for all the observations previously released in DR15 and prior releases (e.g. the flux calibration was updated). The emission-line parameters of the spaxel spectra for our sample of galaxies are available from the MaNGA Data Analysis Pipeline (DAP) measurements. We derived the characteristics for a sample of 430 galaxies using the latest version of the DAP measurements (manga-n-n-MAPS-SPX-MILESHC-MASTARSSP.fits.gz[1] for the spectral data and the Data Reduction Pipeline (DRP) measurements manga-n-n-LOGCUBE.fits.gz[2] for the photometric data).

We selected a sample of galaxies using the following criteria. First, we chose the discy galaxies for which the curves of isovelocities in the measured line-of-sight velocity fields resemble a set of parabola-like curves (hourglass appearance of the rotation disc). This condition provides a possibility to determine the geometric parameters of a galaxy, which are necessary for determining the galactocentric distances of individual spaxels and constructing radial distributions of the characteristics across the galaxy. Using this criterion, we also rejected strongly interacting and merging galaxies in which the line-of-sight velocity field is distorted to such an extent that the determination of the geometrical angles and rotation curve is impossible. Second, galaxies with an inclination angle larger than ~70° were rejected because the fit of the Hα velocity field in such galaxies can produce unrealistic values of the inclination angle (Epinat et al. 2008), and, consequently, the estimated galactocentric distances of the spaxels can involve large uncertainties; moreover, the interpretation of the abundance in individual spaxel is not beyond the question since the spaxel spectra involves radiations that originated in volumes at different galactocentric distances along the line of sight. Third, we considered MaNGA galaxies mapped with 91 and 127 fibre IFUs, covering 27.″5 and 32.″5 on the sky (with a large number of spaxels over the galaxy image). We only chose galaxies for which the spaxels with measured emission lines are well distributed across galactic discs and cover more than ~0.8 R_{25}.

The determination of the geometrical galaxy parameters (the coordinates of the rotation centre, the position angle of the major kinematic axis, and the inclination angle), rotation curve, surface-brightness profile, optical radius of the galaxy, radial distributions of the oxygen abundance, and other characteristics are described in detail in our previous papers (Pilyugin et al. 2018, 2019, 2020, 2021). In brief, the geometrical parameters of the galaxy and the rotation curve are derived by best fitting the observed line-of-sight velocity field using an iterative procedure (Pilyugin et al. 2019). The galactocentric distances of the spaxels determined with the obtained coordinates of the rotation centre of the galaxy and kinematic angles were used to construct the radial distributions of the oxygen and nitrogen abundances and other characteristics across the disc of the galaxy. The measurements in the SDSS filters g and r for each spaxel were converted into B-band magnitudes following Pilyugin et al. (2018). The radial surface-brightness distribution was fitted within the optical radius by a broken exponential profile for the disc and by

---

[1] `https://data.sdss.org/sas/dr17/manga/spectro/analysis/v3_1_1/3.1.0/SPX-MILESHC-MASTARSSP/`

[2] `https://dr17.sdss.org/sas/dr17/manga/spectro/redux/v3_1_1/`

a general Sérsic profile for the bulge:

$$
\begin{aligned}
I(r) &= I_{\rm e}\exp\{-b_{\rm n}[(r/r_{\rm e})^{1/{\rm n}}-1]\} \\
&+ I_{0,\rm inner}\exp(-r/h_{\rm inner}) \quad if \quad r < R^{*}, \\
&= I_{\rm e}\exp\{-b_{\rm n}[(r/r_{\rm e})^{1/{\rm n}}-1]\} \\
&+ I_{0,\rm outer}\exp(-r/h_{\rm outer}) \quad if \quad r > R^{*}.
\end{aligned}
\qquad (1)
$$

Here, R^{*} is the break radius, i.e. the radius at which the exponent changes. The eight parameters, $I_{\rm e}$, $r_{\rm e}$, n, $(\Sigma_{\rm L})_{0,\rm inner}$, $h_{\rm inner}$, $(\Sigma_{\rm L})_{0,\rm outer}$, $h_{\rm outer}$, and R^{*}, in the broken exponential disc were determined through the best fit to the observed surface-brightness profile. The value of the isophotal radius, $R_{25,}$ was estimated using the fit corrected for the galaxy inclination.

The distances to the galaxies were taken from the NASA/IPAC Extragalactic Database (NED)[3]. The NED distances use flow corrections for Virgo, the Great Attractor, and Shapley Supercluster infall (adopting a cosmological model with H_0 = 73 km/s/Mpc, $\Omega_{\rm m}$ = 0.27, and Ω_Λ = 0.73). We adopted the spectroscopic stellar masses of the Sloan Digital Sky Survey (SDSS) and BOSS (BOSS stands for the Baryon Oscillation Spectroscopic Survey in SDSS-III, see Dawson et al. 2013). The spectroscopic masses were taken from the table STELLARMASSPCAWISCBC03 and were determined using the Wisconsin method (Chen et al. 2012) with the stellar population synthesis models from Bruzual & Charlot (2003). The reported errors in the values of the stellar mass are usually within 0.15–0.2 dex.

The measured line fluxes were corrected for the interstellar reddening using the reddening law of Cardelli et al. (1989) with $R_{\rm V}$ = 3.1. We classified the excitation of the spaxel spectrum using its position on the standard diagnostic Baldwin–Phillips–Terlevich (BPT) diagram: [N II]λ6584/Hα versus the [O III]λ5007/Hβ, as suggested by Baldwin et al. (1981). As in our previous studies (Pilyugin et al. 2020, 2021; Pilyugin & Tautvaišienė 2024), the spectra located to the left (below) the demarcation line of Kauffmann et al. (2003b) are referred to as the SF-like or H II-region-like spectra; those located to the right of (above) the demarcation line of Kewley et al. (2001) are referred to as the AGN-like spectra; and the spectra located between both demarcation lines are classified as intermediate (INT) spectra.

The oxygen abundances in spaxels with H II-region-like spectra were determined through the R calibration from Pilyugin & Grebel (2016). The calibration relation for H II regions with log$N_2 \geq -0.6$ (the upper branch) is

$$
\begin{aligned}
({\rm O/H})^{*}_{\rm R} &= 8.589 + 0.022\,\log(R_3/R_2) + 0.399\,\log N_2 \\
&+ (-0.137 + 0.164\,\log(R_3/R_2) + 0.589\log N_2)\,, \\
&\times \log R_2
\end{aligned}
\qquad (2)
$$

and the relation for H II regions with log$N_2 < -0.6$ (the lower branch) is

$$
\begin{aligned}
({\rm O/H})^{*}_{\rm R} &= 7.932 + 0.944\,\log(R_3/R_2) + 0.695\,\log N_2 \\
&+ (0.970 - 0.291\,\log(R_3/R_2) - 0.019\log N_2)\,, \\
&\times \log R_2
\end{aligned}
\qquad (3)
$$

where $({\rm O/H})^{*}_{\rm R}$ = 12 +log(O/H)$_{\rm R}$, and standard notations for the fluxes $R_2 = I_{[\rm O\,II]\lambda3727+\lambda3729}/I_{\rm H\beta}$, $N_2 = I_{[\rm N\,II]\lambda6548+\lambda6584}/I_{\rm H\beta}$, and $R_3 = I_{[\rm O\,III]\lambda4959+\lambda5007}/I_{\rm H\beta}$ are used. The nitrogen-to-oxygen ratios were estimated using the corresponding calibration relation from Pilyugin & Grebel (2016):

$$
\begin{aligned}
\log\,({\rm N/O}) &= -0.657 - 0.201\,\log N_2 \\
&+ (0.742 - 0.075\,\log N_2) \times \log(N_2/R_2).
\end{aligned}
\qquad (4)
$$

2.2. Galaxy sample

By visual inspection of the oxygen abundance maps for 430 galaxies, we find five galaxies that show distinct azimuthal asymmetry in the abundance in the sense that in the inner part (more than a half of the optical radius R_{25} of the galaxy) of each galaxy there is a sector-like (semi-circle in one case) region where the oxygen abundance (O/H)$_{\rm h}$ is higher than the abundance (O/H)$_{\rm l}$ in other sector: M-8450-12701 (with a region of azimuthal O/H asymmetry within 0.5 R_{25}), M-8546-12704 (with a region of azimuthal O/H asymmetry within 0.7 R_{25}), M-8561-12701 (with a region of azimuthal O/H asymmetry within 0.5 R_{25}), M-9500-09102 (with a region of azimuthal O/H asymmetry within 0.6 R_{25}), and M-11761-12705 (with a region of azimuthal O/H asymmetry within 0.9 R_{25}). Fig. 1 shows oxygen abundance maps for the selected target galaxies with azimuthal O/H asymmetry. The galaxy M-12078-12705 with the more or less symmetrical oxygen abundance (control galaxy) is shown in panel (f) of Fig. 1 for comparison. The characteristics of the target galaxies are reported in Table 1. These galaxies were investigated in the current study.

Galaxies M-8450-12701, M-8561-12701, and M-9500-09102 are isolated galaxies, the galaxy M-11761-12705 is a member of a pair of galaxies (Tempel et al. 2018). The M-8546-12704 is an isolated galaxy according to Tempel et al. (2018). However, the Sc galaxy (PGC 2412032, SBS 1552+524B, where SBS is the Second Byurakan Survey) is located at the distance of $\sim 2.'7$ in the sky plane corresponding to ∼41 kpc at the adopted distance. The difference in the line-of-sight velocities is $\Delta V_{\rm los} \sim$ 81 km s^{-1}. This suggests that M-8546-12704 is not an isolated galaxy but a member of a galaxy pair.

Panel (a) of Fig. 2 shows the oxygen abundance in the spaxel as a function of radius for M-8450-12701. The radial distribution of the oxygen abundances is usually fitted by the linear relation of the type 12 +log(O/H) = (O/H)$_0$ + grad × R/R_{25}, where (O/H)$_0$ = 12 + log(O/H)$_{\rm R=0}$ is the central oxygen abundance, and the gradient is expressed in units of dex R_{25}^{-1}. The radial abundance distribution in M-8450-12701 should be fitted by the broken linear relation with the break at R/R_{25} = 0.77. The mean deviation of the points from the O/H – R relation is around 0.05 dex. The points with the deviations larger than 0.15 dex (3σ) are not used in the determination of the final O/H – R relation. The parameters (O/H)$_0$ and grad for the relations inside and outside break radius are reported in Table 1. The obtained (O/H) – R relation is shown by the line in the panel (a) of Fig. 2.

One can see in panel (a) of Fig. 2 that the oxygen abundances in the inner part of the galaxy ($R \lesssim 0.5R_{25}$) do not form a single sequence along the radius; instead, they are split into two branches. Abundances of both the upper branch, (O/H)$_{\rm h}$, and the lower branch, (O/H)$_{\rm l}$, are concentrated on two levels of the abundance. Panel (b) of Fig. 2 shows the normalised histogram of the oxygen abundances for the spaxels within region of azimuthal O/H asymmetry (<0.5R_{25}). The solid line denotes the histogram of the obtained oxygen abundances. The histogram demonstrates two distinct peaks in the abundance distribution for the spaxels in the inner part of the galaxy. The Pearson's χ^2 test shows that the null hypothesis can be rejected at the level of p < 0.01. Fitting this distribution by two Gaussians (the dashed red line in panel (b) of Fig. 2), we found the peak of high abundances (upper branch) is at 12+log(O/H)$_{\rm h}$ = 8.586, and the peak of the low abundances (lower branch) is at 12+log(O/H)$_{\rm l}$ = 8.501.

Figures 3–6 show the oxygen abundance as a function of radius and the normalised histogram of the oxygen abundances for the spaxels in the region of azimuthal O/H asymmetry

---

[3] NED is operated by the Jet Populsion Laboratory at the California Institute of Technology, under contract with NASA. `http://ned.ipac.caltech.edu/`

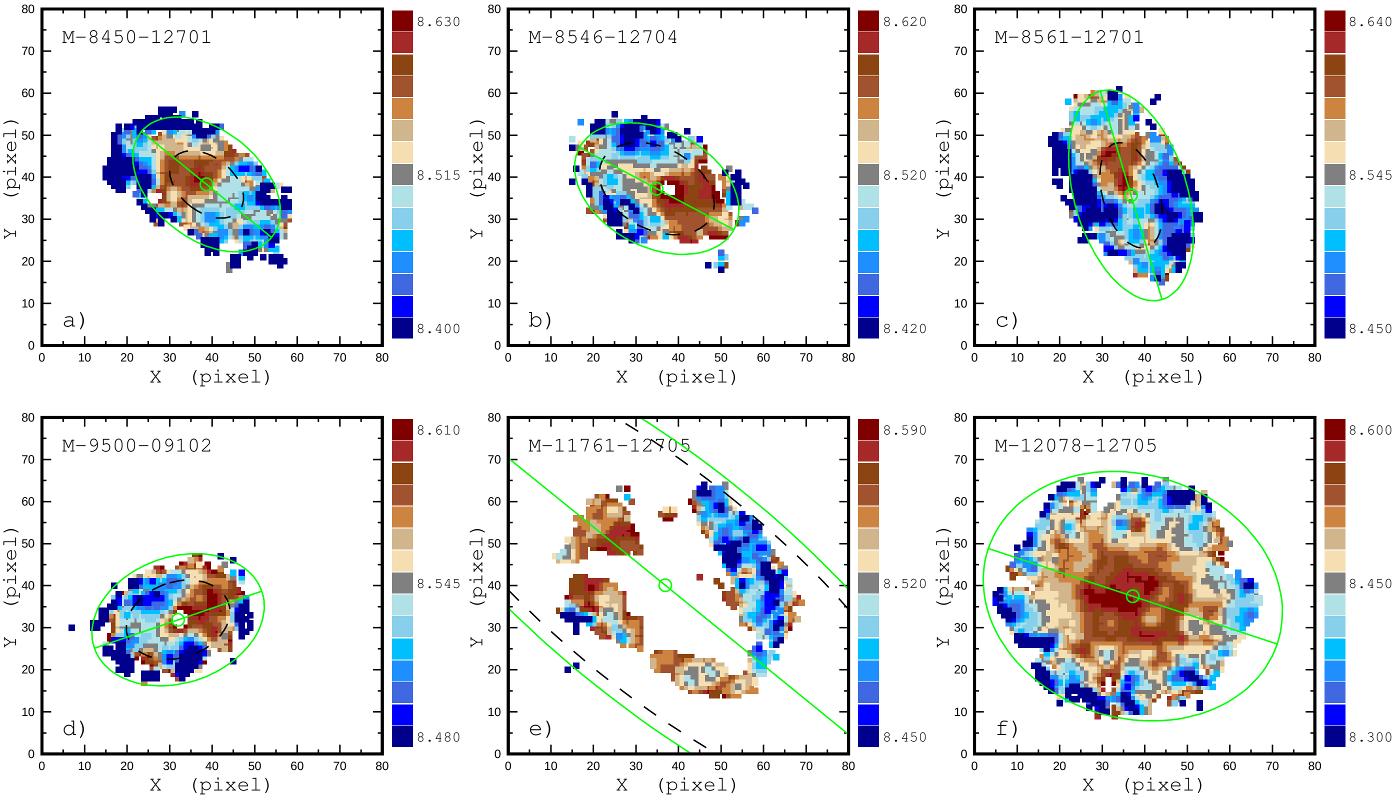

Fig. 1. Oxygen abundance maps for our sample of selected target MaNGA galaxies with azimuthal asymmetry in the abundance distribution across the galaxy and control galaxy. Each panel shows the distribution of the oxygen abundance across the image of the galaxy in sky coordinates (pixels). The value of the oxygen abundance in the spaxel is colour-coded. The circle shows the kinematic centre of the galaxy, the line indicates the position of the major kinematic axis of the galaxy, and the solid ellipse is the optical radius. The dashed ellipse shows the area considered in the current study. *Panels a, b, c, d, and e* show the target galaxies; *panel f* displays the control galaxy.

Table 1. Characteristics$^{(a)}$ of the MaNGA galaxies of our sample.

Galaxy ID	d Mpc	$\log M_\star$ $M_\odot$	R_{25} Kpc	(O/H)$_\mathrm{h}$ 12+log(O/H)	(O/H)$_\mathrm{l}$ 12+log(O/H)	(O/H)$_0$ 12+log(O/H)	grad dex/R$_{25}$	d(O/H)$_\mathrm{asym}$ dex	SFR $M_\odot$/year	Environ-ment
(1)	(2)	(3)	(4)	(5)	(6)	(7)	(8)	(9)	(10)	(11)
8450 12701	197.4	10.1	9.47	8.586	8.501	8.586$^{(b)}$	−0.098	0.041	–0.304	Isolated
8546 12704	210.5	10.4	10.51	8.592	8.519	8.588	−0.089	0.069	0.275	multu
8561 12701	210.2	10.4	13.15	8.597	8.522	8.581	−0.090	0.053	0.038	Isolated
9500 09102	193.7	10.2	9.77	8.597	8.534	8.580	−0.062	0.042	0.083	Isolated
11761 12705	128.6	11.6	27.56	8.555	8.491	8.586	−0.128	0.030	0.362	multu

Notes. $^{(a)}$ Distance to the galaxy d, stellar mass $M_\star$, optical (or isophotal) radius R_{25}, oxygen abundances of the high (O/H)$_\mathrm{h}$ and the low (O/H)$_\mathrm{l}$ metallicity regions, central oxygen abundance in the galaxy (O/H)$_0$, slope of the metallicity gradient, value of the global azimuthal asymmetry for the whole galaxy d(O/H)$_\mathrm{asym}$, current star formation rate (SFR), and environment. $^{(b)}$ The radial abundance distribution in M-8450-12701 is described by broken relation with the central abundance of (O/H)$_0$ = 8.586 and gradient of −0.098 dex R_{25}^{-1} at $R/R_{25} < 0.77$ and (O/H)$_0$ = 8.829 and gradient of −0.415 dex R_{25}^{-1} at $R/R_{25} > 0.77$.

(radii of regions were reported above) for other target galaxies: M-8546-12704 (Fig. 3), M-8561-12701 (Fig. 4), M-9500-09102 (Fig. 5), and M-11761-12705 (Fig. 6). The radial abundance distribution in each galaxy is approximated by the single linear relation. The histograms demonstrate two distinct peaks in the abundance distribution for each target galaxy. The Pearson's χ^2 test shows that the null hypothesis can be rejected at the level of $p < 0.01$ for each target galaxy. The obtained characteristics of these galaxies (parameters (O/H)$_0$ and grad for the O/H – R relation, the peak values of the high (O/H)$_\mathrm{h}$ and the low (O/H)$_\mathrm{l}$ abundances in the normalised histogram) are listed in Table 1.

We also determined the global azimuthal asymmetry in the oxygen abundance distribution across the whole disc of each target galaxy and the control galaxy following Zinchenko et al. (2016). We divided a galaxy into two semi-circles by a dividing line at a position angle φ. For a fixed value of the angle φ, we determined the arithmetic mean of the deviations d(O/H)$_1$ from the O/H – R relation for spaxels with azimuthal angles from φ to $\varphi + 180$ (first semi-circle) and the mean deviation d(O/H)$_2$ for spaxels with azimuthal angles from $\varphi + 180$ to $\varphi + 360$ (second semi-circle). The absolute value of the difference d(O/H)$_\mathrm{asym}$ = d(O/H)$_1$ – d(O/H)$_2$ was estimated for different values of φ (see Fig. 7). The position of φ was counted anticlockwise from the

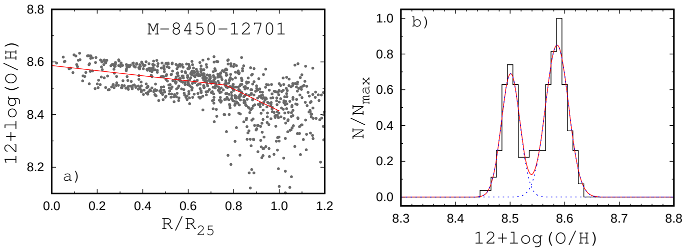

Fig. 2. Oxygen abundance in galaxy M-8450-12701. *Panel a*: Oxygen abundance in individual spaxel determined using R calibration from Pilyugin & Grebel (2016) as a function of radius (points). The line shows the broken linear relation for the radial abundance distribution within optical radius. *Panel b*: Normalised histogram of oxygen abundances for spaxels within the region of distinct azimuthal asymmetry ($<0.5\,R_{25}$ for this galaxy). The solid line denotes the histogram of the obtained oxygen abundances. The dashed red curve corresponds to the fit by two Gaussians to those data, the blue dotted curves show individual Gaussians.

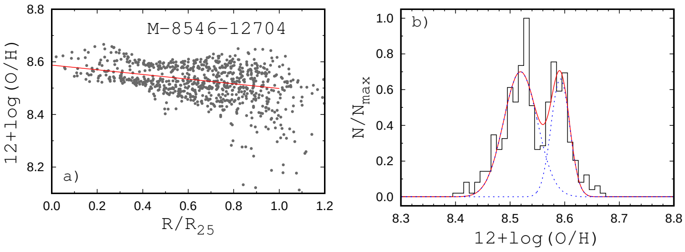

Fig. 3. Same as Fig. 2, but for galaxy M-8546-12704.

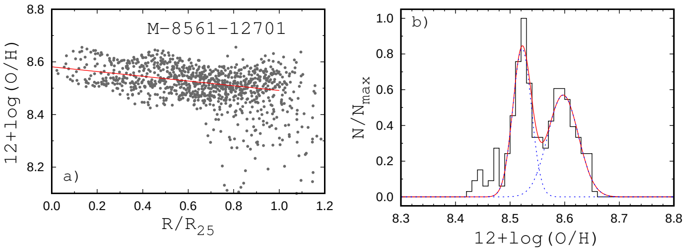

Fig. 4. Same as Fig. 2, but for galaxy M-8561-12701.

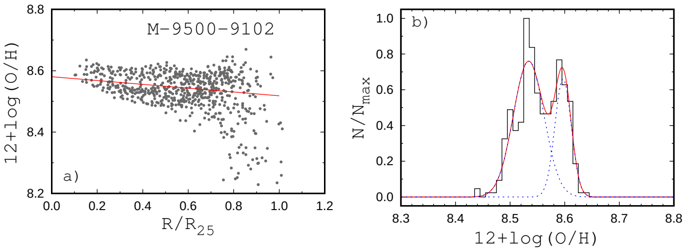

Fig. 5. Same as Fig. 2, but for galaxy M-9500-9102.

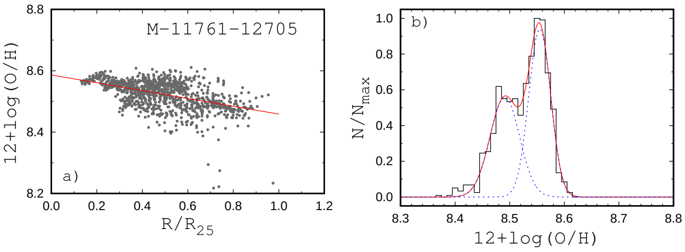

Fig. 6. Same as Fig. 2, but for galaxy M-11761-12705.

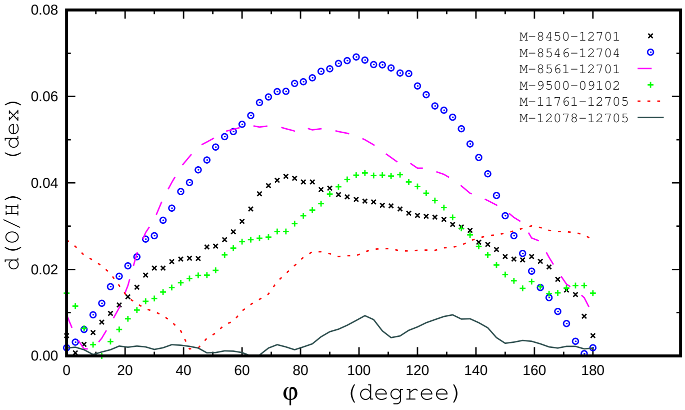

Fig. 7. Global azimuthal asymmetry in oxygen abundance distribution across the whole disc of each target galaxy and control galaxy (M-12078-12705). The lines and symbols show the absolute value of difference between the arithmetic means of the deviations from the O/H – R relation for the spaxels within the sector, with azimuthal angles from φ to $\varphi + 180$ and from $\varphi + 180$ to $\varphi + 360$ as a function of angle φ.

major kinematic axis and changed with a step size of 3° in the computations. The maximum absolute value of the difference d(O/H)$_{\rm asym}$ was used to specify the global azimuthal asymmetry in the abundance distribution across the whole galaxy. The obtained values of d(O/H)$_{\rm asym}$ are reported in Table 1. The value of the d(O/H)$_{\rm asym}$ for the control galaxy is below 0.01, Fig. 7. This is in line with the conclusion in Zinchenko et al. (2016) that the values of azimuthal asymmetry in galaxies are usually within 0.02. The values of the d(O/H)$_{\rm asym}$ for the target galaxies range from ∼0.03 to ∼0.07 and are higher than in the control galaxy. However, the value of the global azimuthal O/H asymmetry for the whole galaxy d(O/H)$_{\rm asym}$ is lower than the difference between the high and low abundances in the region of distinct azimuthal O/H asymmetry d(O/H)$_{\rm h,l}$ = (O/H)$_{\rm h}$ – (O/H)$_{\rm l}$. This is not surprising since the values of the d(O/H)$_{\rm asym}$ and the d(O/H)$_{\rm h,l}$ should be close to each other if only the area of enhanced oxygen abundances coincides with the semi-circle; this is not the case for target galaxies (see Fig. 1).

3. Discussion

3.1. Galaxies with azimuthal abundance asymmetry among other galaxies

Here, we compare our sample of galaxies with azimuthal abundance asymmetry to other galaxies. Firstly, we examined the evolutionary status of our galaxies; that is, we considered their positions in the stellar mass versus star formation rate diagram. We estimated the global star formation rate from the Hα luminosity of a galaxy $L_{\rm H\alpha}$ using the calibration relation of Kennicutt (1998) reduced by Brinchmann et al. (2004) for the Kroupa initial mass function (Kroupa 2001). The Hα luminosity of a galaxy $L_{\rm H\alpha}$ was determined as a sum of the Hα luminosities of the spaxels with H II-region-like spectra within the optical radius. Speagle et al. (2014) investigated the evolution of the star-forming galaxy main sequence in the SFR – $M_\star$ diagram using a compilation of 25 studies from the literature. They found the 'consensus' relation SFR = $f(M_\star, t)$. The SFRs in galaxies with azimuthal abundance asymmetry agree with the SFR – $M_\star$ relation for the present-day epoch (t = 13.6 Gyr).

Next, we compare the central oxygen abundance (O/H)$_0$ and the oxygen abundance at the optical radius (O/H)$_{R_{25}}$ abundances in the galaxies with azimuthal abundance asymmetry and

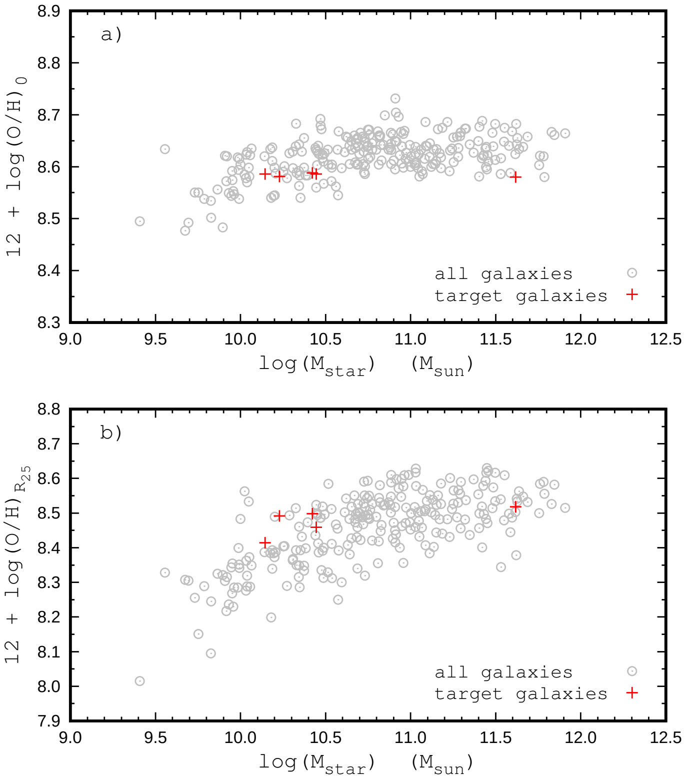

Fig. 8. Comparison of oxygen abundances in galaxies with global azimuthal asymmetry with that in other galaxies. The central oxygen abundance (O/H)$_0$ (*panel a*) and the oxygen abundance at the optical radius (O/H)$_{R_{25}}$ (*panel b*) as a function of the stellar mass are shown. The grey points stand for the comparison galaxies. The plus signs show the galaxies with an azimuthal abundance asymmetry.

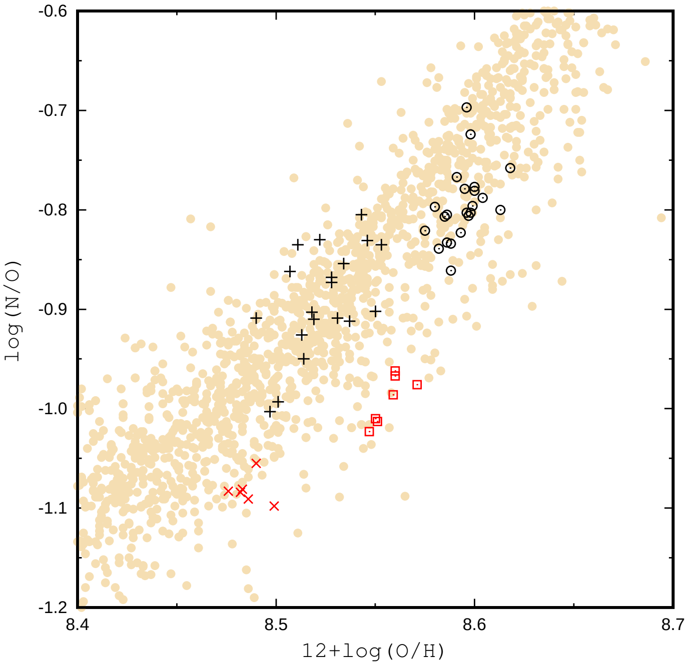

Fig. 9. Locations of high- and low-metallicity regions of galaxies with azimuthal abundance asymmetry in the N/O – O/H diagram. The circles designate the (O/H)$_\mathrm{h}$ regions in the moderate-mass galaxies, and the plus signs show the (O/H)$_\mathrm{l}$ regions in these galaxies. The squares denote the (O/H)$_\mathrm{h}$ regions in the massive galaxy M-11761-12705, and the crosses mark the (O/H)$_\mathrm{l}$ regions in this galaxy. The yellow points show H II regions in nearby galaxies (compilation in Pilyugin & Grebel 2016).

in other galaxies, Fig. 8. The oxygen abundance in the high-metallicity region in the galaxies with azimuthal O/H asymmetry, (O/H)$_\mathrm{h}$, is close to central oxygen abundance. Inspection of the upper panel of Fig. 8 shows that the (O/H)$_0$ in the massive galaxy M-11761-12705 is lower than the central oxygen abundances in galaxies of similar masses, while the (O/H)$_0$ in four moderate-mass galaxies is comparable to the (O/H)$_0$ in galaxies of similar masses. This indicates that the origin of the high-metallicity regions in the massive galaxy M-11761-12705 and four moderate-mass galaxies can be different. An examination of the lower panel of Fig. 8 shows that the (O/H)$_{R_{25}}$ in the massive galaxy M-11761-12705 is located in the lower envelope of the band in the $M_\star$ – (O/H)$_{R_{25}}$ diagram, while the (O/H)$_l$ of four moderate-mass galaxies is located in the upper envelope of the band.

The N/O value for a given O/H contains important information about the enrichment history of heavy elements in the region. The N/O – O/H (or N/H–O/H) diagram has been a subject of many investigations (Edmunds & Pagel 1978; Pilyugin 1992, 1993; Gavilán et al. 2006; Pilyugin & Thuan 2011; Vincenzo et al. 2016; Berg et al. 2019; Schaefer et al. 2020, 2022; Roy et al. 2021; Johnson et al. 2023, among many others). Since the nitrogen production is secondary at high metallicities ($12 + \log(\mathrm{O/H}) \gtrsim 8.0$) then the nitrogen-to-oxygen ratio increases with metallicity at high oxygen abundances. Fig. 9 shows the positions of the high- and low-metallicity regions of our sample of galaxies in the O/H – N/O diagram. The position of the region in the O/H – N/O diagram is mainly defined by three factors. First, the N/O value at a given O/H is dependent on the star formation history (e.g. Edmunds & Pagel 1978; Pilyugin 1992; Pilyugin & Thuan 2011; Maiolino & Mannucci 2019; Romano 2022). Since oxygen and nitrogen are produced in stars of different masses, there is a significant time delay between the release of oxygen, which is mainly produced in massive stars, and that of nitrogen, which is produced in intermediate- and low-mass stars, into the interstellar medium. The N/O ratio of a region is an indicator of the time that has elapsed since the last episode of star formation. When the bulk of the nitrogen-producing stars from previous generations complete their evolution, the nitrogen abundance reaches a high level and the region is located in the upper envelope of the O/H – N/O diagram.

Second, galactic winds alter the N/O abundance ratio in the region (e.g. Pilyugin 1993; Vincenzo et al. 2016) and other characteristics of galaxies (e.g. Dekel & Silk 1986; Mac Low & Ferrara 1999; Sharda et al. 2021). The galactic wind may consist of two parts: the ordinary galactic wind and the enriched galactic wind. Galactic winds are caused by the collective effect of supernova explosions. The ordinary galactic wind is the ambient interstellar medium leaving the galaxy. Some part of supernova ejecta may also leave the galaxy as a part of the galactic wind that drove them. This part of supernova ejections can be called the enriched galactic wind because the supernova ejecta are enriched in heavy elements. The enriched galactic winds result in an increase of the N/O abundance ratio because the supernova ejecta are the main source of the enrichment of the interstellar medium in oxygen, while they do not make a significant contribution to the nitrogen enrichment. The ordinary galactic winds also result in an increase in N/O abundance ratio, because the nitrogen ejected by the long-lived intermediate- and low-mass stars of previous star generations is mixed with the smaller amount of interstellar gas compared to oxygen ejected by massive stars of those generations. One can say that the fraction of oxygen produced by previous star generations leaving

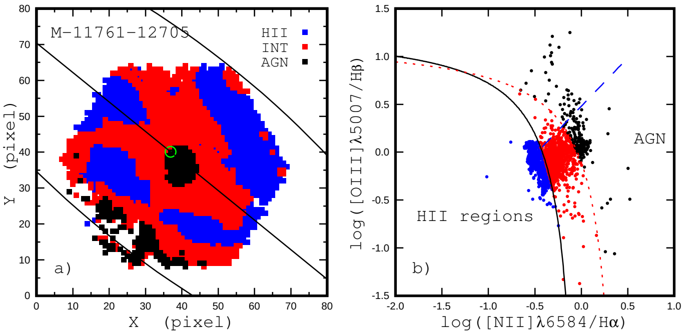

Fig. 10. BPT types of spaxel spectra of MaNGA galaxy M-11761-12705. *Panel a*: Map of BPT types of spaxel spectra. The BPT radiation types for individual spaxels are colour-coded. The circle shows the kinematic centre of the galaxy, the line indicates a position of the major kinematic axis of the galaxy, and the ellipse is the optical radius. *Panel b*: BPT diagram for individual spaxels with H II-region-like (blue), intermediate (red), and AGN-like (black) spectrum classification. The solid and short-dashed curves mark the demarcation line between AGNs and H II regions defined by Kauffmann et al. (2003b) and Kewley et al. (2001), respectively. The long-dashed line is the dividing line between Seyfert galaxies and LINERs defined by Cid et al. (2010).

the galaxy through the ordinary galactic winds is higher than the fraction of nitrogen produced by those star generations.

Third, the infall of low-metallicity (pristine) gas into the region changes its position in the N/O – O/H diagram (Köppen & Hensler 2005; Maiolino & Mannucci 2019). Indeed, the pristine gas mixed to the ambient interstellar gas reduces the absolute values of the nitrogen and oxygen abundances, but it does not change the N/O ratio.

An inspection of Fig. 9 shows that the positions of the high- and low-metallicity regions in the massive galaxy M-11761-12705 and moderate-mass galaxies in the O/H – N/O diagram are significantly different. Since the star formation history and efficiency of galactic winds are correlated with the galactic mass, the locations of galaxies of different masses in the O/H – N/O diagram are different, with higher-mass systems having higher N/O at a fixed O/H (Pérez-Montero et al. 2013; Schaefer et al. 2022). However, the position of the massive galaxy M-11761-12705 with azimuthal abundance asymmetry does not follow this trend.

3.2. Origin of the azimuthal abundance asymmetry in the massive galaxy M-11761-12705

It was noted above that there is evidence that the origin of the high- and low-metallicity regions in the massive galaxy M-11761-12705 and in moderate-mass galaxies can be different. Here, we consider the giant galaxy M-11761-12705, which has a stellar mass of $\log(M_\star/M_\odot) = 11.6$. The field of view of the MaNGA observation only covers a part of M-11761-12705. A large fraction of the individual spaxels do not show the H II-region-like spectra; in particular, the galaxy hosts the central AGN (see Fig. 10). The oxygen abundances can be estimated in the spaxels with the H II-region-like spectra. As a result, abundance map does not cover the whole field of view of the MaNGA observation (see panel (e) in Fig. 1).

The central oxygen abundance in M-11761-12705 is lower than the central oxygen abundances in galaxies of similar masses. The high- and low-metallicity regions in M-11761-12705 are located in the very low envelope of the band outlined by H II regions in nearby galaxies in the O/H – N/O diagram in Fig. 9. This is just opposite the expected location, since massive galaxies are usually well advanced in their (chemical) evolution and occupy the upper envelope of the band in the O/H – N/O diagram (Pérez-Montero et al. 2013; Schaefer et al. 2022; Pilyugin & Tautvaišienė 2024).

One can suggest a simple scenario for the origin of unusual abundances in M-11761-12705. As other massive galaxies, M-11761-12705 was well advanced in its (chemical) evolution, converting a bulk of its gas into stars. The low-metallicity gas infall took place onto the galaxy, decreasing the abundance in the ambient interstellar gas. The subsequent starburst occurred some time ago, between 20 Myr $\lesssim t \lesssim$ 50 Myr. This time is sufficient for the massive stars to end their evolution as supernova explosions and to enrich the interstellar medium with oxygen. At the same time, a bulk of the nitrogen-producing stars do not have enough time to complete their evolution and eject nitrogen into the interstellar medium (see e.g. Fig. 1 in Maiolino & Mannucci 2019). As a result, the N/O ratio becomes very low. The gas infall onto M-11761-12705 and starburst can be caused by the interaction with another galaxy. Indeed, M-11761-12705 is a member of the galaxy pair (Tempel et al. 2018). The interaction is also confirmed by the high value of the asymmetry parameter, A, (see below). Our scenario is similar to that considered by Pérez-Díaz et al. (2024). They found that massive luminous infrared galaxies are located in the low envelope of the band in the O/H – N/O diagram. Pérez-Díaz et al. (2024) concluded that their positions can be caused by an infall of metal-poor gas eventually followed by a rapid enrichment.

3.3. Origin of the azimuthal abundance asymmetry in moderate-mass galaxies of our sample

The stellar masses of four galaxies in our sample of galaxies with azimuthal abundance asymmetry lie in the range from $\log(M_\star/M_\odot) = 10.1$ (galaxy M-8450-12701) to $\log(M_\star/M_\odot) = 10.4$ (galaxy M-8561-12701). Here, we analyse properties of those galaxies in order to understand the origin of the azimuthal asymmetry in abundance.

In each galaxy, the radial abundance distributions within the high- and low-metallicity regions are flat (the abundances are at approximately constant levels). The positions of high-metallicity regions of the galaxies M-8450-12701, M-8561-12701, and M-9500-09102 in the N/O – O/H diagram are closer to the lower envelope of the band outlined by the H II regions in nearby galaxies than the positions of low-metallicity regions of those galaxies, Fig. 9. This effect is less evident for the galaxy M-8546-12704.

The simultaneous enhancement of the oxygen abundance in high-metallicity region and shift of its position towards the low envelope in the N/O – O/H diagram in comparison to the low-metallicity region cannot be explained by the continuous star formation; instead, those facts together suggest that the enrichment in oxygen and nitrogen should be attributed to the starburst in the high-metallicity region. If the starburst occurred several dozens Myr ago, a large number of massive stars ended their evolution and enriched the interstellar medium with oxygen (producing a jump-like enhancement of the oxygen abundance), while many nitrogen-producing stars do not have enough time to complete their evolution and eject nitrogen into the interstellar medium (resulting in the shift towards the lower envelope in the N/O – O/H diagram). The difference in oxygen abundances between the high-metallicity and low-metallicity regions of 0.08 dex corresponds to the change in the gas-mass fraction (astration level) of ~0.06. The amount of stellar mass

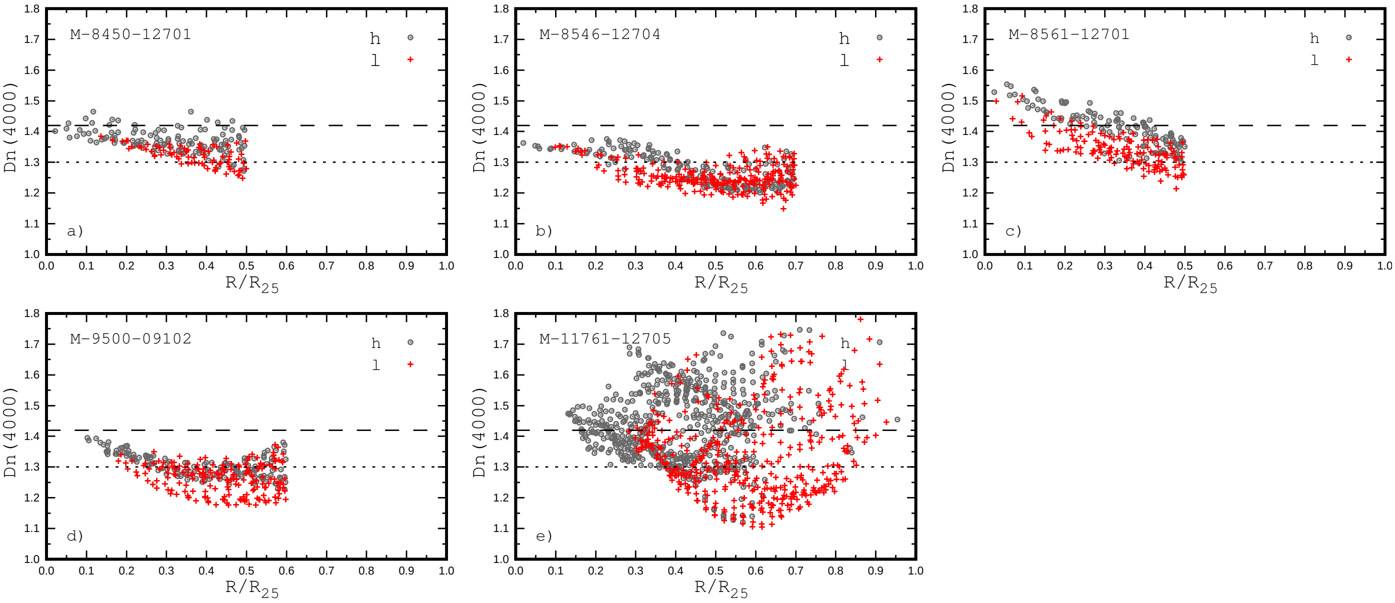

Fig. 11. Spectral index $D_n(4000)$ for individual spaxel as a function of radius for our sample of galaxies. The grey circles denote the spaxels of the high-metallicity regions, the red plus signs are the spaxels of the low-metallicity regions. The dashed line marks $D_n(4000) = 1.42$, and the dotted line shows $D_n(4000) = 1.3$ (see text).

formed during the starburst can range from several to several dozens percentage (French et al. 2018; Reeves & Hudson 2024).

Thus, the origin of the bimodality of oxygen abundances in galaxies with azimuthal asymmetry can be the following. The oxygen and nitrogen abundances were uniform (similar to those in the low-metallicity region) in the whole galaxy. An episode of high star formation (starburst) occurred several dozens of Myr ago in a large region, increasing the oxygen abundance and (temporarily) decreasing the nitrogen-to-oxygen ratio in this region.

The spectral index $D_n(4000)$ (the ratio of the average flux density in the bands 3850–3950 and 4000–4100 Å) can serve as a proxy for the look-back time of the starburst (e.g. French et al. 2018; Wu et al. 2023). French et al. (2018) noted that the relation between $D_n(4000)$ and the post-burst age suffers from a degeneracy with the burst mass fraction and burst duration. They find that for post-starbursts with $D_n(4000) < 1.3$, where post-starburst ages are typically under 300 Myr, the degeneracy is lessened, and $D_n(4000)$ is highly correlated with the post-burst age. However, if $D_n(4000) > 1.42$, where post-starburst ages typically range from 300 to 1500 Myr, $D_n(4000)$ is no longer significantly correlated with the post-burst age.

Figure 11 shows the spectral index $D_n(4000)$ for individual spaxels as a function of the radius for our sample of galaxies. The grey circles denote the spaxels of high-metallicity regions, the red plus signs are the spaxels of low-metallicity regions. An inspection of Fig. 11 shows that the spectral index $D_n(4000)$ is higher in the spaxels of high-metallicity regions than in the spaxels of low-metallicity regions; that is, the ages of the stellar populations are higher in the spaxels of high-metallicity regions than in the spaxels of low-metallicity regions. The galaxy M-8561-12701 shows most clearly that the spectral index $D_n(4000)$ is higher in the spaxels of high-metallicity regions than in those of low-metallicity regions (see panel (c) of Fig. 11). This is in conflict with the assumption that the enhancement of oxygen abundance in the high-metallicity region should be attributed to the starburst that occurred several dozens Myr ago. Fig. 12 shows the current star formation rate surface density for individual spaxels as a function of the radius for our sample of galaxies. Fig. 12 shows that the current star formation rate is higher in the spaxels of low-metallicity regions than in those of high-metallicity regions. Again, the galaxy M-8561-12701 shows this difference most clearly. A comparison between panel (c) of Fig. 11 and panel (c) of Fig. 12 shows that the spectral indices of $D_n(4000)$ are lower in spaxels with the high current star formation rate than in spaxels with the low current star formation rate. This can be considered as evidence that the spectral index $D_n(4000)$ for the individual spaxel can be significantly affected by current star formation and is not a very reliable indicator of stellar age.

If the assumption about the starburst in the high-metallicity region several dozens of Myr ago should be rejected based on the behaviour of the $D_n(4000)$ indices, the higher oxygen abundance in the high-metallicity region together with the shift of its position towards the low envelope in the N/O – O/H diagram compared to the low-metallicity region should be explained in an alternative way: the star formation in the galaxy is accompanied by galactic winds, and the region that evolved with the higher efficiency of the enriched galactic winds shows lower metallicity. It was discussed above that the enriched galactic winds decrease the O/H abundance and increase the N/O abundance ratio in the region. Galactic winds are strongly dependent on $M_\star$, star formation rate, and characteristics of the interstellar medium (Hayward & Hopkins 2017; Marasco et al. 2023). In the contemporary Universe, strong winds are only observed in galaxies undergoing intense bursts of star formation (Heckman et al. 2015). There is a star formation rate threshold for the generation of galactic winds, $\Sigma_{\rm SFR} \sim 0.1 M_\odot$ yr^{-1} kpc^{-2} (Heckman 2001) or $\Sigma_{\rm SFR} \sim 0.01 M_\odot$ yr^{-1} kpc^{-2} (López-Cobá et al. 2019). It should be noted that $\Sigma_{\rm SFR} \sim 0.1 M_\odot$ yr^{-1} kpc^{-2} is the dividing value of the SFR between the non-starbursting and starbursting galaxies (Kennicutt & De Los Reyes 2021).

Thus, the higher oxygen abundance in the high-metallicity region together with the shift in its position towards the low envelope in the N/O – O/H diagram compared to the low-metallicity region can be explained in two alternative ways. First, the starburst in the high-metallicity region occurred several dozens of Myr ago. Second, the star formation in the galaxy

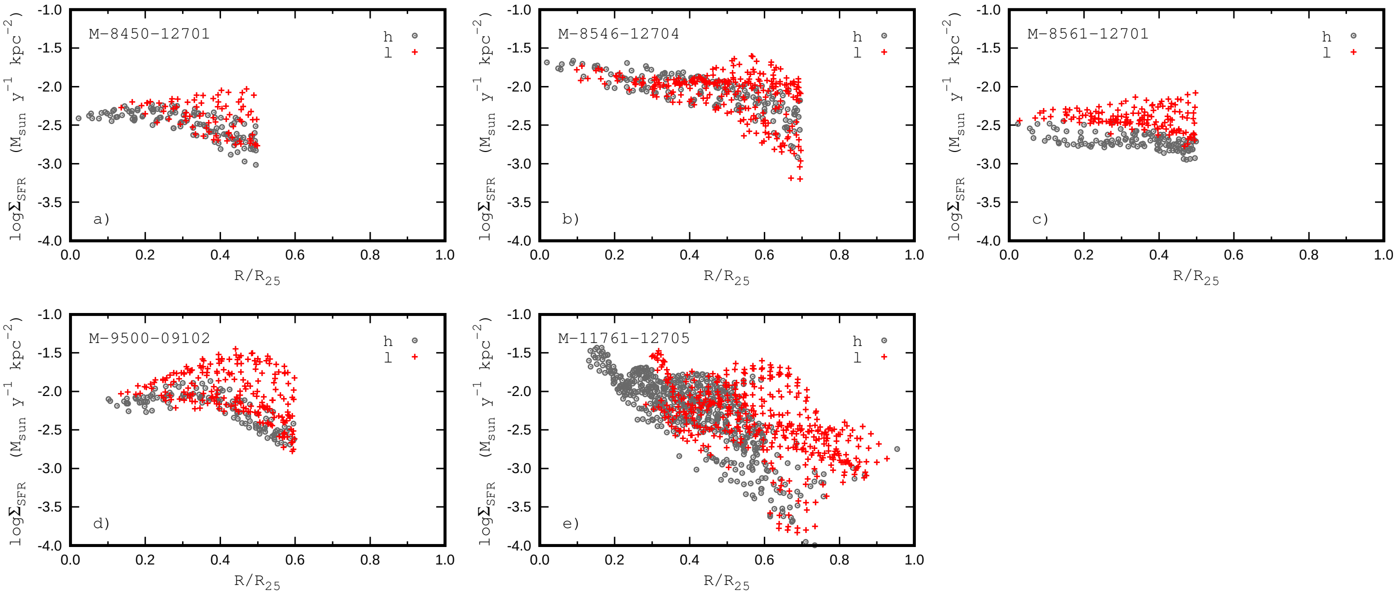

Fig. 12. Star formation surface density for individual spaxel as a function of radius for our sample of galaxies. The grey circles denote the spaxels of the high-metallicity regions, and the red plus signs show the spaxels of the low-metallicity regions.

is accompanied by the galactic winds, and the region evolved with the lower efficiency of the enriched galactic winds shows higher metallicity. It should be noted that both scenarios suggest episodes of high star formation (starburst). This suggests that the flat abundance distributions (abundances at a nearly constant level) in the regions of moderate-mass galaxies are related to the bursty star formation. Of course, our sample of four galaxies is too small to draw a solid conclusion, and further investigations are necessary to confirm or reject this conclusion.

3.4. Mergers and interactions

Despite extensive observational and theoretical studies, the physical mechanisms that regulate the star formation rates of galaxies are still poorly understood (e.g. Yesuf et al. 2017). Therefore, an important question, that is, why the (chemical) evolutions of two sectors of the galaxy with azimuthal abundance asymmetry differ, cannot be answered. However, if there is any other distinctive characteristic common to all these galaxies, it could be a hint as of the necessary condition for the origin of those galaxies. Currently, there is a belief that galaxy-galaxy interactions and mergers can have a significant effect on galaxy evolution, altering different characteristics of a galaxy. In particular, the interaction and merger can result in the enhancement of the star formation rate (Barton et al. 2000; Lotz et al. 2008; Pawlik et al. 2016, among many others). It is predicted that the galaxy-galaxy interactions and mergers can produce a flat abundance gradient (Rupke et al. 2010a; Sillero et al. 2017; Bustamante et al. 2018; Sharda et al. 2021), and observations show that the merging and interacting systems exhibit shallow oxygen abundance gradients compared to isolated spiral galaxies (Rupke et al. 2010b; Kewley et al. 2010; Rosa et al. 2014; Croxall et al. 2015; Torres-Flores et al. 2020). Here, we examine whether our galaxies with azimuthal abundance asymmetry show signs of interactions or mergers. It should be noted that we selected a sample of discy galaxies for which the curves of iso-velocities in the measured line-of-sight velocity fields resemble a set of parabola-like curves (hourglass appearance of the rotation disc). Using this criterion, we rejected strongly interacting and merging galaxies if the line-of-sight velocity field was distorted to such an extent that the determination of the geometrical angles and rotation curve was impossible. Therefore, our sample can only include the interacting and merging galaxies where the distortion of the line-of-sight velocity field is not crucial.

The most common way to identify galaxy mergers and interactions is by morphology. The asymmetry parameter, A, quantifies the asymmetry of a light distribution across the galaxy (Schade et al. 1995; Conselice 2003):

$$A = \frac{\sum\limits_{i,j} |I_{ij} - I_{ij}^{180}|}{\sum\limits_{i,j} I_{ij}}, \tag{5}$$

where I_{ij} is the flux of a spaxel in the original image, and I_{ij}^{180} is the flux of the same spaxel after the image has been rotated by 180° around the centre of the galaxy. The sum is carried out on all spixels within the optical radius of the galaxy. We also estimated the indices, R_A, to specify the distribution of residual fluxes (Schade et al. 1995):

$$R_A = \frac{\sum\limits_{i,j} \frac{1}{2}|W_{ij} - W_{ij}^{180}|}{\sum\limits_{i,j} I_{ij}}, \tag{6}$$

where W_{ij} is a residual spaxel flux[4] after the model flux is subtracted: $W_{ij} = I_{ij}^{\rm obs} - I_{ij}^{\rm mod}$. The model flux in the spaxel was estimated from the photometric profile using Eq. (1). The determined value of parameters A and R_A for our sample of galaxies are presented in Table 2.

The average value of the asymmetry parameters in early-type spirals (Sa and Sb galaxies) is $A = 0.07 \pm 0.04$; the late-type spirals (Sc and Sd galaxies) show higher asymmetries of $A = 0.15 \pm 0.06$ (Conselice 2003). The high asymmetry value ($A > 0.35$) can serve as an indicator of the merger or interaction (Conselice 2003; Wilkinson et al. 2022). A galaxy is classified as ‘asymmetric’ if $R_A > 0.05$ (Schade et al. 1995).

---

[4] We used the symbol W to designate the residual flux in the individual spaxel instead of the commonly used symbol R, since it already used here to designate the galactocentric distance of the spaxel.

Table 2. Asymmetry parameter, A, of a light distribution across the galaxy and index, $R_{A,}$ of the asymmetry in the distribution of the residual fluxes across the galaxy for the MaNGA galaxies of our sample.

MaNGA name	A	R_A
8450 12701	0.241	0.119
8546 12704	0.324	0.179
8561 12701	0.284	0.135
9500 09102	0.306	0.161
11761 12705	0.610	0.307

Two galaxies of our sample (M-8546-12704 and M-11761-12705) are members of galaxy pairs. However, the asymmetry parameter, A, is above the canonical threshold value ($A = 0.35$) for non-interacting/interacting galaxies in the massive galaxy M-11761-12705 only (see Table 2). The values of the A parameter in four moderate-mass galaxies (including the member of the galaxy pair, M-8546-12704) are higher than the average value of the asymmetry parameters in the late-type spirals, but they are below the threshold value. Thus, we cannot make a solid conclusion as to whether the moderate-mass galaxies of our sample show signs of interactions or mergers and whether this is a necessary condition for the origin of those galaxies. At the same time, the values of the asymmetry index R_A, in the distribution of the residual fluxes after the model flux is subtracted is higher than 0.05 in all the galaxies of our sample; that is, each galaxy can be classified as asymmetric.

Galaxy merger/interaction features may persist for up to ~1 Gyr, but gradually fade and become faint ~200 Myr after coalescence (Lotz et al. 2008; Pawlik et al. 2016; Wilkinson et al. 2022). Recently, Bottrell et al. (2024) used the Illustris TNG50 simulation to investigate the relative roles of major mergers (stellar-mass ratios $\mu \gtrsim 0.25$), minor mergers ($0.1 \lesssim \mu < 0.25$), and mini mergers ($0.01 \lesssim \mu < 0.1$) in the evolution of star-forming galaxies. They found that individual mini-merger events yield small enhancements in asymmetries ($\Delta R_A \sim 0.01$) that are sustained on long timescales (~3 Gyr after coalescence, on average). The remnants of major/minor mergers peak at much greater amplitudes ($\Delta R_A \sim 0.03$–0.05), but this enhancement is short-lived (less than ~1 Gyr after coalescence). Moreover, the timing of morphological disturbances is generally offset from the peak in star formation rates, with strong morphological disturbances occurring before bursts of merger-induced star formation (Lotz et al. 2008). Hence, not all merger-induced starbursts exhibit morphological features of the merger.

4. Conclusion

We find five MaNGA galaxies that show distinct azimuthal asymmetry in the abundance across the disc, in the sense that in the inner part (more than half of optical radius R_{25}) of each galaxy there is a sector-like (up to semi-circle) region where the oxygen abundances $(\mathrm{O/H})_\mathrm{h}$ are higher than the abundances $(\mathrm{O/H})_\mathrm{l}$ in the other sector. M-11761-12705 is a massive galaxy with a stellar mass of $\log(M_\star/M_\odot) = 11.6$. The masses of four other galaxies (M-8450-12701, M-8546-12704, M-8561-12701, M-9500-09102) are moderate, within the range of $10.1 \lesssim \log(M_\star/M_\odot) \lesssim 10.4$.

Abundances within high- and low-metallicity regions show flat radial gradients (the abundances are at nearly constant levels in each region). The histogram for the spaxel abundances demonstrates two distinct peaks, and the differences between the peaks are of 0.06–0.08 dex. The high-metallicity regions are usually located in the O/H – N/O diagram closer to the lower envelope of the band outlined by H II regions in nearby galaxies than the low-metallicity regions. The abundance properties in the massive galaxy M-11761-12705 can be explained by the low-metallicity gas infall onto the galaxy and subsequent episode of high star formation rate (starburst) that occurred between 20 Myr $\lesssim t \lesssim 50$ Myr ago in the diluted interstellar medium.

For moderate-mass galaxies, the higher oxygen abundance in the high-metallicity region and its shift towards the lower envelope of the band in the N/O – O/H diagram in comparison to the low-metallicity region can be explained in one of two ways: either the starburst in the high-metallicity region occurred several dozens of Myr ago; or, the star formation in the galaxy is accompanied by the galactic winds, and the region evolved with the lower efficiency of the enriched galactic winds shows higher metallicity. Both scenarios suggest an episode with a high star formation rate (starburst). This suggests that the flat abundance distributions in the regions of moderate-mass galaxies are related to the bursty star formation. However, our sample of four galaxies is too small to make a solid conclusion; further investigations are necessary.

Two galaxies of our sample are members of galaxy pairs. However, the asymmetry parameter, A, quantifying asymmetry of a light distribution across the galaxy, is above the canonical threshold value ($A = 0.35$) for non-interacting/interacting galaxies in the massive galaxy M-11761-12705 only. At the same time, the values of the index R_A of the asymmetry in the distribution of the residual fluxes after a model flux is subtracted are higher than 0.05 in all the galaxies of our sample; that is, each galaxy can be classified as asymmetric.

Acknowledgements. We are grateful to the referee for his/her constructive comments. L.S.P acknowledges support from the Research Council of Lithuania (LMTLT, No. P-LU-PAR-25-8). This research has made use of the NASA/IPAC Extragalactic Database (NED), which is funded by the National Aeronautics and Space Administration and operated by the California Institute of Technology. We acknowledge the usage of the HyperLeda database (`http://leda.univ-lyon1.fr`). Funding for SDSS-III has been provided by the Alfred P. Sloan Foundation, the Participating Institutions, the National Science Foundation, and the U.S. Department of Energy Office of Science. The SDSS-III web site is `http://www.sdss3.org/` Funding for the Sloan Digital Sky Survey IV has been provided by the Alfred P. Sloan Foundation, the U.S. Department of Energy Office of Science, and the Participating Institutions. SDSS-IV acknowledges support and resources from the Center for High-Performance Computing at the University of Utah. The SDSS web site is `www.sdss.org`

References

Abdurro'uf, Accetta, K., Aerts, C., et al. 2022, ApJS, 259, 35
Baldwin, J. A., Phillips, M. M., & Terlevich, R. 1981, PASP, 93, 5
Barton, E. J., Geller, M. J., & Kenyon, S. J. 2000, ApJ, 530, 660
Belfiore, F., Maiolino, R., Tremonti, C., et al. 2017, MNRAS, 469, 151
Bellardini, M. A., Wetzel, A., Loebman, S. R., et al. 2021, MNRAS, 505, 4586
Bellardini, M. A., Wetzel, A., Loebman, S. R., & Bailin, J. 2022, MNRAS, 514, 4270
Berg, D. A., Erb, D. K., Henry, R. B. C., Skillman, E. D., & McQuinn, K. B. W. 2019, ApJ, 874, 93
Berg, D. A., Pogge, R. W., Skillman, E. D., et al. 2020, ApJ, 893, 96
Bottrell, C., Yesuf, H. M., Popping, G., et al. 2024, MNRAS, 527, 6506
Brinchmann, J., Charlot, S., White, S. D. M., et al. 2004, MNRAS, 351, 1151
Bruzual, G., & Charlot, S. 2003, MNRAS, 344, 1000
Bundy, K., Bershady, M. A., Law, D. R., et al. 2015, ApJ, 798, 7
Bustamante, S., Sparre, M., Springel, V., & Grand, R. J. J. 2018, MNRAS, 479, 3381
Cardelli, J. A., Clayton, G. C., & Mathis, J. S. 1989, ApJ, 345, 245
Chen, Y.-M., Kauffmann, G., Tremonti, C. A., et al. 2012, MNRAS, 421, 314

Cid, Fernandes R., Stasińska, G., Schlickmann, M. S., et al. 2010, MNRAS, 403, 1036

Conselice, C. J. 2003, ApJS, 147, 1

Croxall, K. V., Pogge, R. W., Berg, D. A., Skillman, E. D., & Moustakas, J. 2015, ApJ, 808, 42

Dawson, K. S., Schlegel, D. J., Ahn, C. P., et al. 2013, AJ, 145, 10

Dekel, A., & Silk, J. 1986, ApJ, 303, 39

Edmunds, M. G., & Pagel, B. E. J. 1978, MNRAS, 185, 77P

Epinat, B., Amram, P., Marcelin, M., et al. 2008, MNRAS, 388, 500

French, K. D., Yang, Y., Zabludoff, A., & Tremonti, C. A. 2018, ApJ, 862, 2

Gavilán, M., Mollá, M., & Buell, J. F. 2006, A&A, 450, 509

Grand, R. J. J., Springel, V., Kawata, D., et al. 2016, MNRAS, 460, L94

Grasha, K., Chen, Q. H., Battisti, A. J., et al. 2022, ApJ, 929, 118

Gusev, A. S., Pilyugin, L. S., Sakhibov, F., et al. 2012, MNRAS, 424, 1930

Hayward, C., & Hopkins, P. F. 2017, MNRAS, 465, 1682

Heckman, T. M. 2001, ASP Conf. Ser., 240, 345

Heckman, T. M., Alexandroff, R. M., Borthakur, S., Overzier, R., & Leitherer, C. 2015, ApJ, 809, 147

Ho, I.-T., Kudritzki, R.-P., Kewley, L. J., et al. 2015, MNRAS, 448, 2030

Ho, I.-T., Meidt, S. E., Kudritzki, R.-P., et al. 2018, A&A, 618, A64

Johnson, J. W., Weinberg, D. H., Vincenzo, F., Bird, J. C., & Griffith, E. J. 2023, MNRAS, 520, 782

Kauffmann, G., Heckman, T. M., Tremonti, C., et al. 2003b, MNRAS, 346, 1055

Kennicutt, R. C. 1998, ARA&A, 36, 189

Kennicutt, R. C., & De Los Reyes, M. A. C. 2021, ApJ, 908, 61

Kewley, L. J., Dopita, M. A., Sutherland, R. S., Heisler, C. A., & Trevena, J. 2001, ApJ, 556, 121

Kewley, L. J., Rupke, D., Zahid, H. J., Geller, M. J., & Barton, E. J. 2010, ApJ, 721, L48

Köppen, J., & Hensler, G. 2005, A&A, 434, 531

Kreckel, K., Ho, I.-T., Blanc, G. A., et al. 2019, ApJ, 887, 80

Kroupa, P. 2001, MNRAS, 322, 231

Levy, R. C., Bolatto, A. D., & Teuben, P. 2018, ApJ, 860, 92

López-Cobá, C., Sánchez, S. F., Bland-Hawthorn, J., et al. 2019, MNRAS, 482, 4032

Lotz, J. M., Jonsson, P., Cox, T. J., & Primack, J. R. 2008, MNRAS, 391, 1137

Mac Low, M.-M., & Ferrara, A. 1999, ApJ, 513, 142

Maiolino, R., & Mannucci, F. 2019, A&ARv., 27, 3

Makarov, D., Prugniel, P., Terekhova, N., Courtois, H., & Vauglin, I. 2014, A&A, 570, A13

Marasco, A., Belfiore, F., Cresci, G., et al. 2023, A&A, 670, A92

Orr, M. E., Burkhart, B., Wetzel, A., et al. 2023, MNRAS, 521, 3708

Pawlik, M. M., Wild, V., Walcher, C. J., et al. 2016, MNRAS, 456, 3032

Pérez-Díaz, B., Pérez-Montero, E., Fernández-Ontiveros, J. A., Vílchez, J. M., & Amorín, R. 2024, Nat. Astron., 8, 368

Pérez-Montero, E., Contini, T., Lamareille, F., et al. 2013, A&A, 549, A25

Pilyugin, L. S. 1992, A&A, 260, 58

Pilyugin, L. S. 1993, A&A, 277, 42

Pilyugin, L. S., & Grebel, E. K. 2016, MNRAS, 457, 3678

Pilyugin, L. S., & Tautvaišienė, G. 2024, A&A, 682, A41

Pilyugin, L. S., & Thuan, T. X. 2011, ApJ, 726, L23

Pilyugin, L. S., Vílchez, J. M., & Contini, T. 2004, A&A, 425, 849

Pilyugin, L. S., Thuan, T. X., & Vílchez, J. M. 2007, MNRAS, 376, 353

Pilyugin, L. S., Grebel, E. K., & Kniazev, A. Y. 2014, AJ, 147, 131

Pilyugin, L. S., Grebel, E. K., Zinchenko, I. A., et al. 2018, A&A, 613, A1

Pilyugin, L. S., Grebel, E. K., Zinchenko, I. A., Nefedyev, Y. A., & Vílchez, J. M. 2019, A&A, 623, A122

Pilyugin, L. S., Grebel, E. K., Zinchenko, I. A., et al. 2020, A&A, 639, A96

Pilyugin, L. S., Cedrés, B., Zinchenko, I. A., et al. 2021, A&A, 653, A11

Reeves, A. M. M., & Hudson, M. J. 2024, MNRAS, 527, 2037

Romano, D. 2022, A&ARv., 30, 7

Rosa, D. A., Dors, O. L., Krabbe, A. C., et al. 2014, MNRAS, 444, 2005

Roy, A., Dopita, M. A., Krumholz, M. R., et al. 2021, MNRAS, 502, 4359

Rupke, D. S. N., Kewley, L. J., & Barnes, J. E. 2010a, ApJ, 710, 156

Rupke, D. S. N., Kewley, L. J., & Chien, L.-H. 2010b, ApJ, 723, 1255

Sakhibov, F., Zinchenko, I. A., Pilyugin, L. S., et al. 2018, MNRAS, 474, 1657

Sánchez, S. F., Kennicutt, R. C., Gil de Paz, A., et al. 2012, A&A, 538, A8

Sánchez, S. F., Rosales-Ortega, F. F., Iglesias-Páramo, J., et al. 2014, A&A, 563, A49

Sánchez, S. F., Galbany, L., Pérez, E., et al. 2015, A&A, 573, A105

Sánchez-Menguiano, L., Sánchez, S. F., Pérez, I., et al. 2016, A&A, 587, A70

Sánchez-Menguiano, L., Sánchez, S. F., Pérez, I., et al. 2017, A&A, 603, A113

Sánchez-Menguiano, L., Sánchez, S. F., Pérez, I., et al. 2018, A&A, 609, A119

Sánchez-Menguiano, L., Sánchez, S. F., Pérez, I., et al. 2020, MNRAS, 492, 4149

Schade, D., Lilly, S. J., Crampton, D., et al. 1995, ApJ, 451, L1

Schaefer, A. L., Tremonti, C., Belfiore, F., et al. 2020, ApJ, 890, L3

Schaefer, A. L., Tremonti, C., Kauffmann, G., et al. 2022, ApJ, 930, 160

Searle, L. 1971, ApJ, 168, 327

Sharda, P., Krumholz, M. R., Wisnioski, E., et al. 2021, MNRAS, 504, 53

Sillero, E., Tissera, P. B., Lambas, D. G., & Michel-Dansac, L. 2017, MNRAS, 472, 4404

Smith, H. E. 1975, ApJ, 199, 591

Speagle, J. S., Steinhardt, C. L., Capak, P. L., & Silverman, J. D. 2014, ApJS, 214, 15

Tempel, E., Kruuse, M., Kipper, R., et al. 2018, A&A, 618, A81

Torres-Flores, S., Amram, P., Olave-Rojas, D., et al. 2020, MNRAS, 494, 2785

Vila-Costas, M. B., & Edmunds, M. G. 1992, MNRAS, 259, 121

Vincenzo, F., Belfiore, F., Maiolino, R., Matteucci, F., & Ventura, P. 2016, MNRAS, 458, 3466

Wilkinson, S., Ellison, S. L., Bottrell, C., et al. 2022, MNRAS, 516, 4354

Williams, T. G., Kreckel, K., Belfiore, F., et al. 2022, MNRAS, 509, 1303

Wu, P.-F., Bezanson, R., D'Eugenio, F., et al. 2023, ApJ, 955, 75

Yesuf, H. M., French, K. D., Faber, S. M., & Koo, D. C. 2017, MNRAS, 469, 3015

Zaritsky, D., Kennicutt, R. C., & Huchra, J. P. 1994, ApJ, 420, 87

Zinchenko, I. A., Pilyugin, L. S., Grebel, E. K., Sánchez, S. F., & Vílchez, J. M. 2016, MNRAS, 462, 2016